Research Square

Preprints are preliminary reports that have not undergone peer review.
They should not be considered conclusive, used to inform clinical practice,
or referenced by the media as validated information.

Caloric Constraint During Refeeding Optimizes the Neuroprotective Efficacy of Alternate-Day Fasting

Han Zhan
South China University of Technology
Yaping Zhang
South China University of Technology
Yousi Wen
South China University of Technology
Bin Mou
South China University of Technology
Miaoting Li
South China University of Technology
Liting Zhang
South China University of Technology
Xia Wang
South China University of Technology
Lang Huang
South China University of Technology
Thiruma V. Arumugam
La Trobe University
Zongqin Xiang
South China University of Technology
Yong U. Liu
eyliuy@scut.edu.cn

South China University of Technology

Research Article

Keywords:

Posted Date: March 16th, 2026

DOI: https://doi.org/10.21203/rs.3.rs-9081929/v1

License: This work is licensed under a Creative Commons Attribution 4.0 International License.
Read Full License

Additional Declarations: No competing interests reported.

Abstract

Intermittent fasting (IF) confers neuroprotective effects in models of neurodegeneration, yet whether compensatory caloric intake during refeeding limits these benefits remains unclear. Here we combine longitudinal in vivo two-photon imaging with transcriptomic profiling in a TDP-43 proteinopathy mouse model to resolve the temporal dynamics of alternate-day fasting (ADF). Neuronal degeneration and microglial engagement oscillated with fasting–feeding cycles, decreasing during fasting but increasing during refeeding. Transcriptomic analyses revealed that refeeding triggered a rapid activation of metabolic and biosynthetic programs alongside inflammatory signaling, while suppressing fasting-induced neuroprotective pathways, indicating acute sensitivity of the neuroimmune axis to caloric transitions. Constraining caloric intake during the refeeding phase through a calorie-restricted ADF (crADF) regimen eliminated these oscillatory neuronal and microglial responses. Our findings identify the refeeding phase as a critical determinant of fasting efficacy and show that caloric precision during this window stabilizes neuroimmune homeostasis, thereby enhancing the therapeutic potential of intermittent fasting.

Introduction

Intermittent fasting (IF), particularly alternate-day fasting (ADF), has emerged as a promising intervention for promoting neuroprotection and healthy aging (Campisi et al. 2019; Hodgson et al. 2020). ADF operates through rhythmic metabolic switching (Mattson 2025), activating cellular stress resistance pathways during fasting (Chalkiadaki and Guarente 2012; Shimazu et al. 2013; Abdel-Rahman et al. 2024) while engaging anabolic and plasticity-related programs during refeeding (Liu and Sabatini 2020; Imada et al. 2024; Zhang et al. 2026). However, whether this cyclic metabolic transition uniformly benefits neural systems remains unclear. Although the refeeding phase is traditionally viewed as a restorative period, the rapid metabolic surge driven by compensatory hyperphagia (Anson et al. 2003; Kliewer et al. 2015) may induce a transient metabolic overshoot that counteracts protective adaptations established during fasting (O'Keefe et al. 2008; Thaler et al. 2012).

Current understanding of ADF largely derives from endpoint histological and behavioral analyses (Halagappa et al. 2007; Dias et al. 2021; Pan et al. 2022). Such measurements provide limited temporal resolution and therefore cannot capture dynamic neuroimmune fluctuations occurring across fasting–refeeding cycles. In addition, behavioral assessments are typically conducted during the feeding window to ensure comparable satiety across experimental groups (Zhao et al. 2024). While these measurements demonstrate the cumulative benefits of ADF, they do not resolve whether the refeeding phase itself induces transient neuroimmune perturbations that may offset fasting-associated protection.

To address this question, we performed longitudinal in vivo two-photon imaging to track neuroimmune dynamics with daily resolution. Using a multi-fluorescent labeling strategy to simultaneously monitor neuronal fate and microglial behavior in the same cortical fields, we reveal that neurodegeneration and microglial activity oscillate in synchrony with fasting–refeeding cycles. Transcriptomic profiling further

identifies refeeding-induced metabolic and inflammatory activation that coincides with rapid suppression of fasting-associated neuroprotective programs. Importantly, restricting caloric intake during the refeeding phase stabilizes neuroimmune dynamics and enhances the neuroprotective efficacy of ADF.

Methods

Animals

All animal experiments were conducted in accordance with the guidelines of the Institutional Animal Care and Use Committee (IACUC) of South China University of Technology (Approval No. AEC-2020025). For *in vivo* imaging, *Cx3cr1*$^{GFP/GFP}$ (Stock No. 005582, The Jackson Laboratory) were bred in-house, and male heterozygous offspring (*Cx3cr1*$^{GFP/+}$) were utilized. Specific dietary regimens were initiated at 8 weeks of age according to experimental grouping. Following a 2-month intervention period, mice underwent surgical procedures and subsequent longitudinal *in vivo* imaging. For RNA-seq experiments, wild-type C57BL/6J mice were purchased from the Guangdong Medical Laboratory Animal Center (Guangzhou, China). Similarly, these mice were subjected to the assigned dietary protocols for 2 months starting at 8 weeks of age, prior to surgical procedures and tissue collection. All mice were housed in groups of 3–5 per cage at South China University of Technology. Animals were maintained under controlled environmental conditions (20–25°C; 40–50% humidity; 12-h light/12-h dark cycle) with free access to water and standard chow diet, except for mice subjected to alternate-day fasting (ADF) or calorie-restricted ADF (crADF) protocols, which were restricted as described below.

Dietary interventions

All mice were maintained with unrestricted access to water throughout the study. Three specific dietary regimens were implemented: **Adlibitum (AL) feeding**, mice had continuous, unrestricted access to standard laboratory chow. Food hoppers were monitored and replenished weekly to prevent depletion. **Alternate-day fasting (ADF)**, this regimen consisted of recurring cycles of 24-hour fasting followed by 24-hour *ad libitum* feeding. Fasting phases were initiated at 17:00 by removing all chow and clearing bedding of residual crumbs. Food was reintroduced at 17:00 on the following day. Adherence to the schedule was rigorously documented. **Calorie-restricted alternate-day fasting (crADF)**, the crADF protocol followed the same temporal schedule as the ADF group (24-hour fasting / 24-hour feeding) but with a strict quantitative restriction during the feeding window. At the time of food reintroduction (17:00), the food allotment was calculated based on the number of mice per cage, set at 3.0 g per mouse, a quantity approximating the average daily intake observed in the AL group (Fig. 5a). To minimize errors while ensuring sufficient provision, a positive tolerance of + 0.1 g per mouse was permitted during weighing, while negative errors were prohibited. This regimen assumes an approximate equipartition of food among group-housed cage animals.

Experimental design and animal cohorts

To accommodate the distinct requirements of longitudinal *in vivo* imaging versus transcriptomic profiling, experimental cohorts were organized into two sub-studies with tailored enrollment strategies.

Cohorts for longitudinal in vivo imaging

For longitudinal imaging, mice were enrolled in age-matched sequential cohorts and assigned to one of three groups: *ad libitum* (AL), alternate-day fasting (ADF), or calorie-restricted ADF (crADF). The AL and ADF cohorts initiated their respective dietary regimens at 2 months of age and were maintained on these protocols continuously throughout the surgical and imaging phases to evaluate chronic effects. In contrast, the crADF cohort followed the standard ADF protocol starting at 2 months of age to establish baseline metabolic adaptability; the transition to the specific calorie-restricted regimen occurred 6 days after cranial window implantation.

Cohorts for transcriptomic profiling

For RNA-sequencing analysis, mice were randomly assigned to three groups: AL, ADF-Fasting (ADF-F), and ADF-Refeeding (ADF-RF). To capture distinct metabolic states (fasting vs. refeeding) at a single experimental endpoint, the 48-hour ADF cycles were staggered using a phase-shifted initiation strategy. Specifically, the ADF-RF group initiated their regimen 24 hours later than the ADF-F group. Consequently, at the sample collection endpoint (13:00), the ADF-F group was in the latter stage of the 24-hour fasting window, while the ADF-RF group was in the corresponding phase of the 24-hour refeeding window.

AAV injection and cranial window surgery

Cx3cr1 $^{GFP/+}$ mice were anesthetized with 1.5% isoflurane and placed in a stereotaxic apparatus under aseptic conditions. The surgical procedure began with shaving the scalp and excising a circular piece of skin. The periosteum was removed using hydrogen peroxide followed by a saline rinse. A circular cranial window was created over the M1 cortex using a dental drill. During drilling, bone debris was continuously cleared to maintain a clean surgical field. Following the fenestration, AAV9 CamKIIa::mTDP-43(mutNLS)-linker-mScarlet was injected at the center of the window (coordinates: +1.5 mm ML, ± 1.8 mm AP relative to bregma) at a depth of 0.45 mm from the dura mater. A total of 300 nL of viral suspension was delivered at a rate of 1 nL/s using a microsyringe pump. The pipette was left in place for 10 minutes post-injection to permit adequate viral diffusion. After confirming the skull was dry, a layer of adhesive primer and dental cement was applied to the window edges. A circular glass coverslip was secured over the window, and the cement was solidified using UV light. Finally, a head ring for longitudinal imaging was fixed onto the remaining skull surface with dental cement and stabilized under UV light.

AAV injection for RNA-seq

For transcriptomic analysis, wild type mice underwent stereotaxic viral injection without cranial fenestration. Under 1.5% isoflurane anesthesia and aseptic conditions, AAV9 CamKIIa::mTDP-43(mutNLS)-linker-mScarlet was injected into two cortical regions: the M1 cortex (coordinates: +1.5 mm ML, ± 1.8 mm AP, -0.7 mm DV relative to bregma) and the S1 cortex above the hippocampus (coordinates: -1.6 mm ML, ± 1.5 mm AP, -0.7 mm DV relative to bregma). At each site, 300 nL of viral suspension was delivered at a rate of 1 nL/s. The injection pipette remained in situ for 10 minutes after delivery to ensure proper diffusion before being slowly withdrawn. Following the procedures, the scalp was sutured, and the mice were allowed to recover before returning to their home cages.

Longitudinal in vivo two-photon imaging

In vivo imaging was performed using a Leica Stellaris 8 multiphoton microscope and controlled by Leica LAS X software. Following a 1-week post-surgical recovery period, mice underwent habituation training on a head-fixed treadmill (SITRANTECH, China) to minimize stress-induced motion artifacts during subsequent imaging. Training sessions were conducted for 30 minutes daily for 3 consecutive days, at a time of day consistent with the scheduled imaging window. On imaging days, the microscope system was initialized 1 hour prior to acquisition to ensure stable laser power output. During this warm-up period, mice were acclimatized to the imaging room environment in their home cages with the lid adjusted to allow airflow and olfactory adaptation. Water and food availability during the holding period followed the assigned experimental dietary regimen, with restriction applied only during the brief imaging interval.

For each imaging session, the mouse was head-fixed on the treadmill to minimize movement. The cranial window was gently cleaned with 70% ethanol, and a water reservoir was built around the window using Vaseline to accommodate the water-immersion objective (25×, NA 1.0). The objective was then aligned with the window, and the focal plane was lowered to identify surface vasculature under direct visual observation through the eyepieces. Imaging parameters were set to a resolution of 1024 × 1024 pixels (221 × 221 μm) with a Z-stack depth of 120 μm and a step size of 1 μm. A unidirectional scanning mode was employed to maximize image stability and eliminate jagged edge artifacts. Excitation was performed at 980 nm for simultaneous visualization of mScarlet (TDP-43) and GFP (microglia), with emission signals collected by separate detectors (HyD). Laser power was adjusted between 60 and 150 mW depending on imaging depth. Detector gain was adjusted strictly to maintain visibility for morphological tracking; quantitative intensity analysis was not performed, rendering gain adjustments non-confounding.

For the initial session (Day 1), the field of view (FOV) was selected based on optimal viral expression in the M1 cortex, starting approximately 10–20 μm below the first appearance of labeled neurons. For subsequent longitudinal sessions, the same FOV was re-identified by recognizing the unique spatial constellation of labeled neurons. Given that neuronal positions are relatively fixed and the overall degeneration kinetics were sufficiently gradual over the imaging window, the cellular pattern served as a reliable fiducial marker for re-alignment. Precise registration was achieved using a digital reticle overlay

to strictly align the X, Y, and Z coordinates and rotational angle with the reference image from Day 1. During acquisition, the live image stream was continuously monitored by the operator to detect motion artifacts, and scans were immediately repeated if stability was compromised. Following acquisition, the objective was retracted, and the cranial window was carefully cleaned of Vaseline and moisture before returning the mouse to its cage.

Image preprocessing

Raw Z-stack data acquired over the 7-day imaging window were extracted and organized for computational analysis. Prior to alignment, a quality control (QC) step was implemented to assess fluorescence stability. The global fluorescence intensity of each stack was normalized to its corresponding Day 1 baseline. Sessions exhibiting excessive signal attenuation (signal loss > 25%) were excluded from analysis; however, we ensured that the final dataset retained balanced sample sizes across all experimental groups.

To facilitate efficient computation, raw images underwent a standardized preprocessing pipeline using custom Python scripts accelerated by CuPy (GPU-based computing). Images were spatially downsampled by a factor of 2 and subjected to Gaussian smoothing (sigma = 1 pixel) to reduce noise. Contrast enhancement was applied by clipping the top and bottom 0.35% of pixel intensities to remove outliers, followed by normalization to an 8-bit range.

Automated Z-axis registration strategy

To correct for daily variations in imaging depth and brain tissue deformation, we developed a context-aware Z-alignment algorithm. For the initial time point (Day 1), slice 10 was defined as the reference anchor plane. For subsequent days (Day N), the optimal corresponding Z-plane was determined using a multi-slice template matching approach:

1. Search Window Definition: A 5-slice candidate window (centered on the expected position) from the Day N stack was compared against a corresponding 5-slice reference window from the Day N-1 stack.
2. Rigid Registration: To account for XY-plane shifts, candidate slices were first aligned to the reference using the pystackreg library (rigid body transformation).
3. Similarity Scoring: The structural similarity between aligned slices was quantified using template matching (normalized cross-correlation, cv2.matchTemplate). To avoid edge artifacts caused by translation, the scoring region was cropped by 20% from the image borders.
4. Anchor Update: The slice yielding the highest cumulative correlation score was identified as the new anatomical anchor for Day N, ensuring continuous and precise tracking of the same cortical volume across the 7-day period.

XY-plane registration and motion correction

Following Z-plane optimization, lateral motion artifacts were definitively corrected using the same pystackreg-based rigid-body transformation framework. To maximize processing speed, transformation matrices were computed on the datasets spatially downsampled by a factor of 2. These calculated transformations were then directly applied to the original full-resolution raw images.

We implemented a two-stage registration strategy to ensure global alignment across the longitudinal image series:

1. Reference Stabilization: The Day 1 stack served as the global anatomical reference. To eliminate intra-stack motion artifacts within the reference stack, a sequential registration was performed where each slice z was aligned to the preceding slice z-1, generating a set of stabilization matrices (M_{ref}).
2. Longitudinal registration: For subsequent imaging sessions (Day 2–7), each Z-plane was registered to the corresponding plane of the stabilized Day 1 stack to compute the daily displacement matrices (M_{day}).
3. Composite Transformation: To map all stacks into a unified coordinate system, the final transformation for each slice was derived by computing the dot product of the daily displacement matrix and the reference stabilization matrix ($M_{final} = M_{ref} \cdot M_{day}$). This ensured that all 7-day trajectories were strictly aligned to the stabilized Day 1 cortical volume.

Visual inspection of the registered stacks (e.g., at slice 50) was performed to verify the correction accuracy.

Longitudinal layer extraction and cell segmentation

To systematically analyze neuronal fate, representative optical sections were extracted at fixed intervals (e.g., every 20 μm) from the aligned Z-stacks; this spacing was chosen to minimize the likelihood of sampling the same neuronal somata across adjacent sections. Although global Z-registration was previously applied, we implemented an additional adaptive slice-matching step to correct for any residual local tissue deformations. For each selected reference plane in the Day 1 stack, a local search window was defined for subsequent sessions (Day 2–7) spanning ± 10 slices relative to the corresponding slice index. Within this window, the optimal matching slice was identified by maximizing structural similarity to the Day 1 reference, ensuring precise longitudinal correspondence of cellular features.

The matched longitudinal sequences were then assembled into composite RGB images, with mScarlet (TDP-43) mapped to the red channel and GFP (microglia) to the green channel. To identify individual neurons for subsequent morphological analysis, automated cell segmentation was performed using Cellpose, a generalist deep learning-based segmentation algorithm. The Day 1 mScarlet channel served as the anatomical template for generating neuronal masks, which were subsequently saved and applied to the entire longitudinal series to track specific neuronal trajectories and adjacent microglial activities.

Manual cell fate tracking and classification criteria

Manual tracking was performed to reconstruct longitudinal fate trajectories for individual neurons within each FOV. Given the distinct morphological features of TDP-43 pathology and microglial interaction, classification criteria were rigorously standardized. To ensure strict methodological consistency and eliminate inter-observer variability, all tracking and state assignments were performed by a single investigator.

Neuronal states were defined as follows: (1) "Intact": TDP-43 + neurons exhibiting a robust, large soma with mScarlet fluorescence predominantly localized to the somatic periphery; (2) "Shrunken": neurons displaying significant somatic atrophy with mScarlet signal condensed throughout the reduced cell body relative to intact baselines; and (3) "Phagocytosed": neurons manifesting as *in situ* punctate residues or complete signal loss. Microglial interaction states were categorized as: (1) "Untouched"; (2) "Contacted": microglial processes wrapping the neuron partially; and (3) "Fully engulfed": the neuronal soma being completely surrounded by microglial processes.

A custom-built Graphical User Interface (GUI) was developed to facilitate this large-scale longitudinal analysis. The software imported the preprocessed optical sections and the corresponding Cellpose-generated masks. To ensure comprehensive tracking of all traceable neurons within the FOV, the interface allowed manual addition or deletion of masks to correct any segmentation errors. Leveraging the prior image registration, selecting a specific mask automatically retrieved and displayed the corresponding cropped image series spanning the 7-day observation window. The investigator sequentially reviewed the temporal sequence to assign state labels for each time point. Unique identifiers were assigned to each cell, and classification results were stored in project files, allowing for iterative review. Finally, custom scripts were used to parse these project files and extract single-cell fate trajectories for downstream statistical analysis.

Unsupervised Autoencoder and Latent Space Mapping

To capture the continuous dynamic evolution of neuroimmune interactions rather than relying solely on static endpoint snapshots, we employed an unsupervised deep learning approach to map the high-dimensional temporal data into a visualizable manifold. The input for each cell consisted of a 14-dimensional feature vector, representing the longitudinal trajectory of neuronal state and microglial interaction status over the 7-day imaging period.

We constructed a symmetric autoencoder neural network using the TensorFlow/Keras framework. The encoder compressed the 14-dimensional input through a series of fully connected (dense) layers with decreasing dimensionality (128, 64, and 32 units), utilizing ReLU activation functions. The information was funneled into a 2-dimensional latent bottleneck, where a Sigmoid activation function was applied to constrain the latent coordinates within a normalized range of [0, 1]. The decoder reconstructed the original trajectory from this latent space through symmetrical expanding layers (32, 64, and 128 units; ReLU activation), culminating in a linear output layer matching the original input dimensions.

To prioritize the accurate reconstruction of the final cell fate, we implemented a custom weighted Mean Squared Error (MSE) loss function. Specifically, a penalty weight of $\lambda = 6$ was assigned to the reconstruction error of the terminal time point (Day 7), whereas all other time points carried a unit weight ($\lambda = 1$). The model was trained exclusively on trajectories from the control group to learn the baseline landscape of neurodegeneration, with 20% of the data randomly reserved for validation. Optimization was performed using the Adam algorithm. To ensure robustness, training was repeated multiple times; a representative model demonstrating optimal convergence and latent separation was preserved and subsequently used as a fixed pre-trained encoder to project trajectories from all experimental groups into the same 2D latent space.

Identification of distinct neurodegenerative trajectory subtypes

To objectively categorize the diverse neuronal fates, we performed unsupervised clustering within the generated 2D latent manifold. Specifically, the K-means algorithm was applied to the encoded latent coordinates of the AL training dataset. The number of clusters was set to $k = 6$, a value determined to optimally resolve biologically distinct trajectory patterns ranging from stable survival to rapid degeneration.

Consistent with the dimensionality reduction workflow, the trained K-means model including cluster centroids was serialized and stored. This established a standardized classification reference, allowing trajectory data from other experimental groups (e.g., ADF, crADF) to be mapped and assigned to these pre-defined subtypes without introducing batch-effect variability.

Bulk RNA-sequencing (Sample collection)

At the experimental endpoint, mice designated for transcriptomic analysis were transcardially perfused with ice-cold phosphate-buffered saline (PBS) to remove blood and minimize background interference. To strictly prevent RNA degradation, all surgical instruments and work surfaces were thoroughly treated with RNaseZap prior to tissue processing. Following perfusion, the brain was rapidly extracted. To precisely target the viral transduction area, the brain was sectioned using a coronal brain matrix. The cortical region expressing mScarlet was identified under direct visual observation of fluorescence and dissected. The isolated cortical tissues were immediately transferred into RNase-free 1.5 mL microcentrifuge tubes pre-chilled on ice and snap-frozen in liquid nitrogen to preserve RNA integrity. Upon completion of sampling, specimens were transported on dry ice on the same day to Guangzhou Genedenovo Biotechnology Co., Ltd. for downstream processing.

Statistics

Prism 10.4.0 was used for statistical analysis. Statistical tests used are specified at the end of each figure legend. To evaluate phase-dependent changes within the same experimental group (e.g., fasting versus refeeding windows), a two-tailed ratio paired t-test was applied to the measurements obtained from the same subjects. For comparisons involving multiple experimental groups, the normality and

homogeneity of variance were first assessed. In cases where variances were unequal, Welch's ANOVA or Brown-Forsythe and Welch ANOVA tests were employed, followed by Dunnett's T3 multiple comparisons test for post-hoc analysis. For comparisons between two independent groups, an unpaired two-tailed t-test with Welch's correction was utilized. All quantitative data are presented as mean ± standard error of the mean (SEM). For all tests, statistical significance was predefined as $P < 0.05$.

Results

Microglia participate in the engulfment and phagocytosis of pathological neurons in TDP-43 proteinopathy.

To visualize neuron–microglia interactions during neurodegeneration, we established a longitudinal in vivo imaging platform in a mouse model of TDP-43 proteinopathy (Tziortzouda et al. 2021). Nuclear localization signal (NLS) mutant TDP-43 fused with mScarlet was selectively expressed in cortical neurons via adeno-associated viral (AAV) delivery in Cx3cr1-GFP mice, in which microglia are genetically labeled with GFP (Fig. 1a). Following stereotaxic injection and cranial window implantation, the same cortical fields were imaged daily using two-photon microscopy, enabling longitudinal monitoring of neuronal fate and microglial behavior within individual fields of view (FOVs) (Fig. 1b). Longitudinal imaging revealed progressive morphological alterations in TDP-43–expressing neurons accompanied by dynamic microglial responses. Degenerating neurons frequently exhibited soma shrinkage and were subsequently contacted and engulfed by surrounding microglia (Fig. 1c), suggesting that microglia participate in the clearance of pathological neurons. To systematically characterize these interactions, we established a classification framework capturing both neuronal morphology and microglial engagement. Neurons were categorized as intact, shrunken, or phagocytosed, while microglial interactions were defined as uncontacted, contacted, or fully engulfed (Fig. 1d). Representative longitudinal montages illustrated distinct neuronal trajectories, including neurons that remained intact, underwent shrinkage, or were ultimately engulfed by microglia (Fig. 1e). Population-level analysis revealed a strong association between neuronal degeneration and microglial engagement. Nested distribution analysis showed that intact neurons were largely uncontacted, whereas shrunken and phagocytosed neurons displayed progressively higher levels of microglial interaction (Fig. 1f). Tracking individual neurons over time further revealed coordinated progression of neuronal degeneration and microglial engagement (Fig. 1g). Quantification across the population demonstrated a gradual shift from intact to degenerative states (Fig. 1h), accompanied by increasing microglial interaction and phagocytic activity (Fig. 1i). Together, these findings establish a longitudinal framework for monitoring neuron–microglia dynamics and demonstrate that microglia actively participate in the clearance of degenerating neurons in TDP-43 proteinopathy.

Latent-state analysis resolves trajectories of neuronal degeneration and microglial surveillance.

Given the complex and heterogeneous nature of neuron–microglia interactions observed during longitudinal imaging, conventional metrics based on single morphological features were insufficient to

capture the full spectrum of dynamic neuronal trajectories. To systematically resolve these patterns, we implemented an unsupervised autoencoder framework (Hinton and Salakhutdinov 2006) to compress the 14-dimensional joint state sequences—combining neuronal morphology and microglial interaction across seven consecutive imaging days—into a two-dimensional latent space (Fig. 2a). This dimensionality reduction preserved the temporal progression of neuronal states while enabling visualization of population-level trajectory organization. Projection of individual neurons into this latent space revealed a structured landscape representing their pathological evolution over the imaging period (Fig. 2b). Within this landscape, K-means clustering identified six distinct trajectory clusters, each representing characteristic combinations of neuronal degeneration and microglial engagement. These clusters ranged from relatively stable neuronal states with minimal microglial interaction (Cluster 1) to progressively degenerative states associated with increasing levels of microglial contact and engulfment (Clusters 2, 4, 5, and 6) (Fig. 2c, d). Population-level analysis further demonstrated that clusters differed markedly in the prevalence of microglia–neuron interactions, indicating that microglial surveillance intensifies along degenerative trajectories. Importantly, the latent space exhibited clear biological interpretability. Projection of neuronal survival duration onto the embedding revealed a strong positive correlation with the second encoded dimension (ED2), defining a functional axis that spans from relatively healthy neuronal states to rapidly degenerating neurons (Fig. 2e, f). In contrast, the first encoded dimension (ED1) reflected the degree of microglial surveillance, with increasing values corresponding to higher levels of neuron–microglia interaction and phagocytic engagement (Fig. 2g, h). Thus, the two latent dimensions jointly capture complementary aspects of the neurodegenerative process: neuronal health status and microglial activity. Together, this latent-state framework provides a quantitative representation of neuronal fate trajectories and their associated microglial dynamics during TDP-43 proteinopathy. This approach establishes a sensitive analytical platform for assessing how metabolic interventions reshape the trajectories of neuron–microglia interactions in vivo.

Alternate-day fasting induces phase-dependent oscillations in neurodegeneration and microglial reactivity.

We next applied this quantitative framework to evaluate the impact of Alternate Day Fasting (ADF) on these degenerative trajectories. We subjected mice to a 2-month ADF regimen followed by the same longitudinal imaging protocol (Fig. 3a). Projecting the ADF dataset onto our pre-trained latent landscape revealed a marked global redistribution of neuronal fates: the population shifted toward the healthy Clusters 1 and 2, while the lethal Cluster 6—characterized by rapid degeneration and intense microglial engagement—was robustly suppressed compared to AL controls (Fig. 3b-d). Thus, on a cumulative timescale, ADF effectively truncated the most aggressive neurodegenerative trajectories.

However, resolving these dynamics with single-day precision unmasked a striking phase-dependent volatility. By stratifying events across fasting and refeeding windows, we found that neuroprotective stability was not continuous. Instead, neurodegenerative progression and microglial reactivity oscillated in synchrony with the feeding cycle: the frequencies of neuronal shrinkage (Fig. 3e, f), phagocytosis (Fig. 3g, h), and microglial engulfment (Fig. 3i, j) exhibited a rhythmic surge specifically during refeeding

intervals. This indicates that the sudden caloric influx triggers a metabolic rebound that transiently exacerbates neuronal vulnerability, creating a "two-steps-forward, one-step-back" dynamic that potentially limits the net therapeutic gain.

Refeeding triggers transcriptional overshoot and loss of fasting-induced neuroprotection.

To investigate the molecular basis of the phase-dependent volatility observed in vivo, we profiled cortical transcriptomes across metabolic phases of the ADF cycle. Cortical tissues were collected from ADF mice at the end of fasting (F) or refeeding (RF) periods, together with ad libitum (AL) controls (Fig. 4a). While the RF transcriptome globally resembled the AL state, direct comparison between fasting and refeeding phases yielded the largest number of differentially expressed genes (DEGs) (Fig. 4b), indicating extensive transcriptional reprogramming during the metabolic transition. Analysis of these signatures revealed a characteristic pattern of transcriptional overshoot. Many upregulated genes followed a gradient of F < AL < RF, indicating that refeeding induced expression levels exceeding baseline. These genes included regulators of insulin signaling (Akt2) and lipid metabolism (Fabp7, Apln), consistent with strong metabolic activation during refeeding (Fig. 4c) (Vergadi et al. 2017; Wu et al. 2025; Bertrand et al. 2015). In contrast, genes associated with fasting-induced neuroprotection exhibited a rapid reversal upon refeeding. The fasting phase induced a stress-resilient transcriptional program—including the ketogenic enzyme Hmgcs2, antioxidant metallothioneins (Mt1/2), and adaptive RNA-binding proteins (Cirbp and Rbm3)—which returned to baseline levels during the refeeding phase (Suresh et al. 2025; Subramanian Vignesh and Deepe 2017; Aziz et al. 2025; Hu et al. 2022). Functional enrichment analyses supported this dual molecular transition. Gene Ontology (GO) and KEGG pathway analyses revealed strong enrichment of metabolic processing pathways together with inflammatory signaling (Fig. 4d, e). These findings provide a molecular framework linking the refeeding phase to transient increases in neurodegeneration and microglial activity observed in vivo.

Calorie-restricted refeeding stabilizes neuronal trajectories during alternate-day fasting.

Finally, to determine whether the excess calorie intake of the refeeding phase acts as the primary driver of refeeding-induced neurotoxicity, we aimed to dampen the post-fasting caloric surge. Monitoring of daily food intake confirmed that ADF mice exhibited marked compensatory hyperphagia during the feeding window compared to AL controls (Fig. 5a). To neutralize this, we implemented a calorie-restricted ADF (crADF) strategy, clamping food provision during the refeeding phase to 66% of the unrestricted consumption—a threshold calculated to normalize daily food intake to AL-equivalent levels (Fig. 5b). This intervention yielded profound neuroprotective benefits on a cumulative timescale. Dimensionality reduction revealed that while both ADF and crADF promoted a global shift toward healthy neuronal states (Clusters 1–2) (Fig. 5c, d), crADF demonstrated superior efficacy in forestalling the onset of neurodegeneration and mitigating severe pathology (Fig. 5e). In sharp contrast to the rhythmic surges observed in standard ADF, the frequencies of neuronal shrinkage (Fig. 5f), phagocytosis (Fig. 5g), and microglial engulfment (Fig. 5h) in the crADF cohort were statistically indistinguishable between fasting and feeding windows. Specifically, analysis of the initial disease burden (Day 1) revealed that while

neuronal densities remained comparable between the two fasting groups, the crADF cohort exhibited a distinctly lower prevalence of pathological hallmarks, including shrunken and engulfed neurons (Fig. 6b, e, h). Notably, in terms of these early degenerative events, standard ADF failed to reach statistical significance against AL controls, whereas crADF effectively suppressed the acute manifestations of pathology. Most critically, resolving the temporal dynamics revealed that crADF successfully preserved the beneficial metabolic rhythm without triggering the associated neurotoxicity. While the total incidence of degenerative events over the 7-day window remained comparable across groups (Fig. 6c, f, i), the phase-dependent oscillation was completely abolished in the crADF cohort. Thus, simply limiting caloric intake during the refeeding phase is sufficient to dampen the acute neuroimmune reactivity triggered by metabolic overshoot, thereby unleashing the full therapeutic potential of intermittent fasting.

Discussion

Our findings resolve a critical tension in the metabolic management of neurodegeneration: the apparent paradox between the cumulative benefits of intermittent fasting and the acute risks associated with refeeding. By resolving neuroimmune dynamics with single-day precision, we show that the therapeutic effects of dietary restriction are intrinsically phase-dependent rather than continuous. While fasting suppresses neuroinflammation and stabilizes neuronal states, the refeeding phase—often considered a benign recovery period—can paradoxically exacerbate neuronal vulnerability (de Cabo and Mattson 2019). In the context of TDP-43 proteinopathy, the compensatory hyperphagia characteristic of standard alternate-day fasting (ADF) induces a transcriptional and metabolic overshoot that converts a physiological restoration signal into a transient stressor, promoting neuronal shrinkage and microglial phagocytosis.

This refeeding-associated volatility challenges the prevailing framework used to interpret dietary interventions in neurodegenerative disease. Previous studies demonstrating neuroprotective effects of ADF have primarily focused on cumulative outcomes measured over extended time scales (Ojha et al. 2023; Ye et al. 2024). Such macroscopic analyses obscure short-term fluctuations occurring during the refeeding window. Our longitudinal imaging reveals that these metabolic oscillations represent a potential liability within otherwise beneficial fasting regimens. Mechanistically, a rapid caloric influx may disrupt the delicate balance of metabolic recovery in a vulnerable neural environment, imposing an anabolic load that exceeds adaptive capacity. Consistent with this model, our transcriptomic analyses identify a coordinated molecular transition during refeeding characterized by transcriptional overshoot of metabolic pathways alongside rapid loss of fasting-induced neuroprotective programs.

Importantly, we demonstrate that this vulnerability is modifiable through modulation of the refeeding load. Limiting caloric intake during the refeeding phase effectively stabilizes neuronal trajectories and attenuates microglial reactivity. This principle aligns with the concept of metabolic hormesis, in which beneficial stress responses arise only within a bounded physiological range (Wan et al. 2024). By preventing compensatory hyperphagia, the calorie-restricted ADF (crADF) regimen preserves the beneficial metabolic rhythm while minimizing refeeding-associated neurotoxicity. Conceptually, this

strategy complements the logic of fasting-mimicking diets, which optimize the fasting phase to enhance tissue resilience and regeneration (Brandhorst et al. 2015). Our findings extend this framework by demonstrating that careful management of the refeeding phase is equally critical for maximizing neuroprotective outcomes.

Several limitations should be considered when interpreting these findings. First, our study focuses on TDP-43 proteinopathy and cortical neuronal populations accessible to two-photon imaging. Whether similar phase-dependent dynamics occur in deeper brain structures, such as the hippocampus, or in other aggregate-driven neurodegenerative conditions, including amyloid-β or tau pathology, remains to be determined. Second, although our longitudinal imaging captured day-to-day transitions between metabolic phases, higher temporal resolution will be required to resolve the precise intra-day kinetics of neuronal degeneration and microglial engagement. Finally, metabolic scaling between species warrants careful consideration. Given the substantially higher metabolic rate of mice compared with humans, the 24-hour fasting–refeeding cycle used here likely represents a more extreme physiological perturbation than typical human fasting regimens. Translating these findings to clinical contexts will therefore require careful calibration of refeeding parameters, including caloric magnitude and timing.

In summary, our study highlights the refeeding phase as a previously underappreciated determinant of neuropathological outcomes during dietary restriction. These findings suggest that the therapeutic potential of fasting-based interventions depends not only on the fasting period itself but also on the dynamics of metabolic recovery. By implementing a controlled refeeding strategy, our work provides a conceptual framework for designing dietary interventions that preserve the neuroprotective benefits of metabolic stress while minimizing the detrimental consequences of metabolic volatility.

Declarations

Competing interests

The authors declare no competing interests.

Funding

This work was also supported by the National Key R&D Program of China (Grant No. 2023YFA1800100 to Y.U.L.), the National Natural Science Foundation of China (Grant No. 82071188 to Y.U.L.), the Science and Technology Projects in Guangzhou (Grant No. 2024A03J1256 to Y.U.L.), and Science and Technology Projects in Guangzhou (Grant No. 2025A03J4156 and 2024A04J3932 to Z.X.).

Author Contribution

H.Z., Y.Z. and Y.W. prepared the manuscript with help from other authors. H.Z., Y.Z., Y.W., Z.X. and Y.U.L. conceived and designed this research. H.Z., Y.Z., Y.W., B.M., and Z.X. performed the experiments. H.Z., Y.Z., Y.W., B.M., M.L., Y.L., L.Z., X.W., L.H., T.V.A., Z.X., and Y.U.L. contributed to the discussion and data interpretation. Z.X. and Y.U.L. initiated and supervised the project. H.Z., Y.Z., Y.W., Z.X., and Y.U.L. are the guarantors of this work and, as such, had full access to all the data in the study and take responsibility for the integrity of the data and the accuracy of the data analysis.

Data Availability

No datasets were generated or analyzed during the current study.

References

1. Abdel-Rahman, M., Hussein, A. A., Ahmed-Farid, O. A., Sawi, A. A., & Abdel Moneim, A. E. (2024). Intermittent fasting alerts neurotransmitters and oxidant/antioxidant status in the brain of rats. *Metab Brain Dis, 39*(7), 1291-1305, doi:10.1007/s11011-024-01415-7.
2. Anson, R. M., Guo, Z., de Cabo, R., Iyun, T., Rios, M., Hagepanos, A., et al. (2003). Intermittent fasting dissociates beneficial effects of dietary restriction on glucose metabolism and neuronal resistance to injury from calorie intake. *Proc Natl Acad Sci U S A, 100*(10), 6216-6220, doi:10.1073/pnas.1035720100.
3. Aziz, M., Chaudry, I. H., & Wang, P. (2025). Extracellular Cold-Inducible RNA-Binding Protein: Progress from Discovery to Present. *Int J Mol Sci, 26*(8), doi:10.3390/ijms26083524.
4. Bertrand, C., Valet, P., & Castan-Laurell, I. (2015). Apelin and energy metabolism. *Front Physiol, 6*, 115, doi:10.3389/fphys.2015.00115.
5. Brandhorst, S., Choi, I. Y., Wei, M., Cheng, C. W., Sedrakyan, S., Navarrete, G., et al. (2015). A Periodic Diet that Mimics Fasting Promotes Multi-System Regeneration, Enhanced Cognitive Performance, and Healthspan. *Cell Metab, 22*(1), 86-99, doi:10.1016/j.cmet.2015.05.012.
6. Campisi, J., Kapahi, P., Lithgow, G. J., Melov, S., Newman, J. C., & Verdin, E. (2019). From discoveries in ageing research to therapeutics for healthy ageing. *Nature, 571*(7764), 183-192, doi:10.1038/s41586-019-1365-2.
7. Chalkiadaki, A., & Guarente, L. (2012). Sirtuins mediate mammalian metabolic responses to nutrient availability. *Nat Rev Endocrinol, 8*(5), 287-296, doi:10.1038/nrendo.2011.225.
8. de Cabo, R., & Mattson, M. P. (2019). Effects of Intermittent Fasting on Health, Aging, and Disease. *N Engl J Med, 381*(26), 2541-2551, doi:10.1056/NEJMra1905136.
9. Dias, G. P., Murphy, T., Stangl, D., Ahmet, S., Morisse, B., Nix, A., et al. (2021). Intermittent fasting enhances long-term memory consolidation, adult hippocampal neurogenesis, and expression of longevity gene Klotho. *Mol Psychiatry, 26*(11), 6365-6379, doi:10.1038/s41380-021-01102-4.

10. Halagappa, V. K., Guo, Z., Pearson, M., Matsuoka, Y., Cutler, R. G., Laferla, F. M., et al. (2007). Intermittent fasting and caloric restriction ameliorate age-related behavioral deficits in the triple-transgenic mouse model of Alzheimer's disease. *Neurobiol Dis, 26*(1), 212-220, doi:10.1016/j.nbd.2006.12.019.
11. Hinton, G. E., & Salakhutdinov, R. R. (2006). Reducing the dimensionality of data with neural networks. *Science, 313*(5786), 504-507, doi:10.1126/science.1127647.
12. Hodgson, R., Kennedy, B. K., Masliah, E., Scearce-Levie, K., Tate, B., Venkateswaran, A., et al. (2020). Aging: therapeutics for a healthy future. *Neurosci Biobehav Rev, 108*, 453-458, doi:10.1016/j.neubiorev.2019.11.021.
13. Hu, Y., Liu, Y., Quan, X., Fan, W., Xu, B., & Li, S. (2022). RBM3 is an outstanding cold shock protein with multiple physiological functions beyond hypothermia. *J Cell Physiol, 237*(10), 3788-3802, doi:10.1002/jcp.30852.
14. Imada, S., Khawaled, S., Shin, H., Meckelmann, S. W., Whittaker, C. A., Corrêa, R. O., et al. (2024). Short-term post-fast refeeding enhances intestinal stemness via polyamines. *Nature, 633*(8031), 895-904, doi:10.1038/s41586-024-07840-z.
15. Kliewer, K. L., Ke, J. Y., Lee, H. Y., Stout, M. B., Cole, R. M., Samuel, V. T., et al. (2015). Short-term food restriction followed by controlled refeeding promotes gorging behavior, enhances fat deposition, and diminishes insulin sensitivity in mice. *J Nutr Biochem, 26*(7), 721-728, doi:10.1016/j.jnutbio.2015.01.010.
16. Liu, G. Y., & Sabatini, D. M. (2020). mTOR at the nexus of nutrition, growth, ageing and disease. *Nat Rev Mol Cell Biol, 21*(4), 183-203, doi:10.1038/s41580-019-0199-y.
17. Mattson, M. P. (2025). The cyclic metabolic switching theory of intermittent fasting. *Nat Metab, 7*(4), 665-678, doi:10.1038/s42255-025-01254-5.
18. O'Keefe, J. H., Gheewala, N. M., & O'Keefe, J. O. (2008). Dietary strategies for improving post-prandial glucose, lipids, inflammation, and cardiovascular health. *J Am Coll Cardiol, 51*(3), 249-255, doi:10.1016/j.jacc.2007.10.016.
19. Ojha, U., Khanal, S., Park, P. H., Hong, J. T., & Choi, D. Y. (2023). Intermittent fasting protects the nigral dopaminergic neurons from MPTP-mediated dopaminergic neuronal injury in mice. *J Nutr Biochem, 112*, 109212, doi:10.1016/j.jnutbio.2022.109212.
20. Pan, R. Y., Zhang, J., Wang, J., Wang, Y., Li, Z., Liao, Y., et al. (2022). Intermittent fasting protects against Alzheimer's disease in mice by altering metabolism through remodeling of the gut microbiota. *Nat Aging, 2*(11), 1024-1039, doi:10.1038/s43587-022-00311-y.
21. Shimazu, T., Hirschey, M. D., Newman, J., He, W., Shirakawa, K., Le Moan, N., et al. (2013). Suppression of oxidative stress by β-hydroxybutyrate, an endogenous histone deacetylase inhibitor. *Science, 339*(6116), 211-214, doi:10.1126/science.1227166.
22. Subramanian Vignesh, K., & Deepe, G. S., Jr. (2017). Metallothioneins: Emerging Modulators in Immunity and Infection. *Int J Mol Sci, 18*(10), doi:10.3390/ijms18102197.

23. Suresh, V. V., Sivaprakasam, S., Bhutia, Y. D., Prasad, P. D., Thangaraju, M., & Ganapathy, V. (2025). Not Just an Alternative Energy Source: Diverse Biological Functions of Ketone Bodies and Relevance of HMGCS2 to Health and Disease. *Biomolecules, 15*(4), doi:10.3390/biom15040580.
24. Thaler, J. P., Yi, C. X., Schur, E. A., Guyenet, S. J., Hwang, B. H., Dietrich, M. O., et al. (2012). Obesity is associated with hypothalamic injury in rodents and humans. *J Clin Invest, 122*(1), 153-162, doi:10.1172/jci59660.
25. Tziortzouda, P., Van Den Bosch, L., & Hirth, F. (2021). Triad of TDP43 control in neurodegeneration: autoregulation, localization and aggregation. *Nat Rev Neurosci, 22*(4), 197-208, doi:10.1038/s41583-021-00431-1.
26. Vergadi, E., Ieronymaki, E., Lyroni, K., Vaporidi, K., & Tsatsanis, C. (2017). Akt Signaling Pathway in Macrophage Activation and M1/M2 Polarization. *J Immunol, 198*(3), 1006-1014, doi:10.4049/jimmunol.1601515.
27. Wan, Y., Liu, J., Mai, Y., Hong, Y., Jia, Z., Tian, G., et al. (2024). Current advances and future trends of hormesis in disease. *NPJ Aging, 10*(1), 26, doi:10.1038/s41514-024-00155-3.
28. Wu, L., Ou, G. L., Zhang, W., Ma, H. X., Li, X. Y., Zhen, Y. H., et al. (2025). Fatty acid-binding proteins in cancers. *Int J Surg, 111*(11), 8402-8422, doi:10.1097/js9.0000000000003049.
29. Ye, Y., Fu, C., Li, Y., Sun, J., Li, X., Chai, S., et al. (2024). Alternate-day fasting improves cognitive and brain energy deficits by promoting ketone metabolism in the 3xTg mouse model of Alzheimer's disease. *Exp Neurol, 381*, 114920, doi:10.1016/j.expneurol.2024.114920.
30. Zhang, X., Jiang, T., Wang, C., Montenegro Vazquez, V. F., Wu, D., Yang, X., et al. (2026). Periodic fasting and refeeding re-shapes lipid saturation, storage, and distribution in brown adipose tissue. *PLoS Biol, 24*(1), e3003593, doi:10.1371/journal.pbio.3003593.
31. Zhao, Z., Chen, J. L., Zhan, H., Fang, C. R., Hua, L. B., Deng, H. Y., et al. (2024). Noradrenergic Projections from the Locus Coeruleus to the Medial Prefrontal Cortex Enhances Stress Coping Behavior in Mice Following Long-Term Intermittent Fasting. *Neuromolecular Med, 26*(1), 47, doi:10.1007/s12017-024-08818-w.

Figures

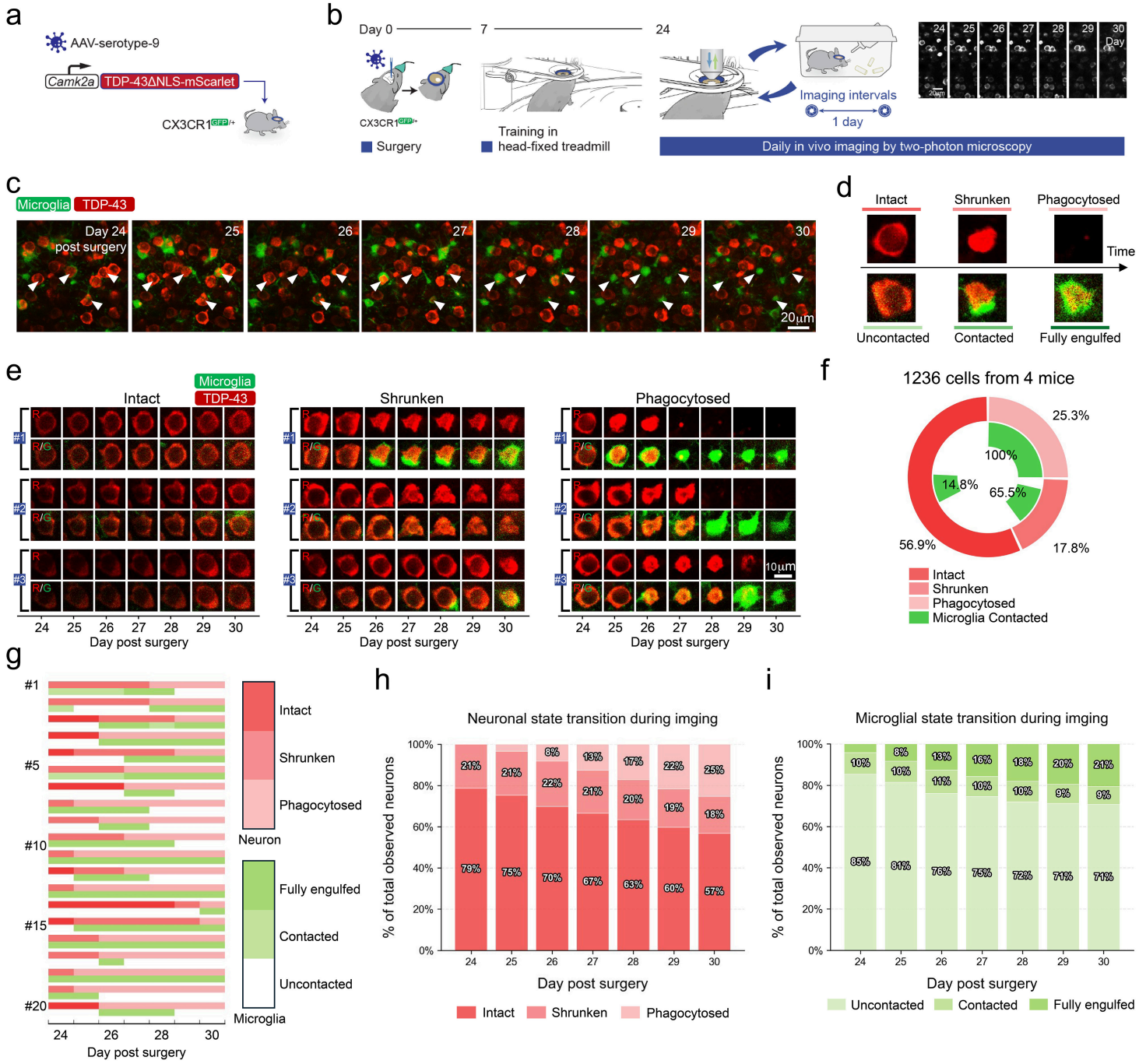


Figure 1

Microglia participate in the engulfment and phagocytosis of pathological neurons in TDP-43 proteinopathy.

a, Schematic of AAV-mediated expression of mScarlet-fused mutant TDP-43 (neurons) in *Cx3cr1*-GFP mice. **b**, Experimental timeline including stereotaxic injection, cranial window implantation, and daily longitudinal two-photon imaging. **c**, Representative longitudinal images tracking the same field of view (FOV) over 7 days; white arrowheads indicate degenerating neurons undergoing microglial engulfment. Scale bar, 20 μm. **d**, Classification criteria for neuronal morphologies (intact, shrunken, phagocytosed) and microglial interaction states (uncontacted, contacted, fully engulfed). **e**, Representative 7-day

montages showing distinct neuronal fates: intact, shrunken, and engulfed. Scale bar, 10 μm. **f**, Nested distribution showing the proportions of distinct neuronal states (outer ring) and the prevalence of microglial interaction within each state (inner ring). **g**, Representative state sequences of 20 neurons tracking the concurrent progression of neuronal degeneration and microglial interaction. **h**, Quantification of the temporal evolution of neuronal state proportions across the analyzed population. **i**, Quantification of the temporal evolution of microglial interaction state proportions across the analyzed population.

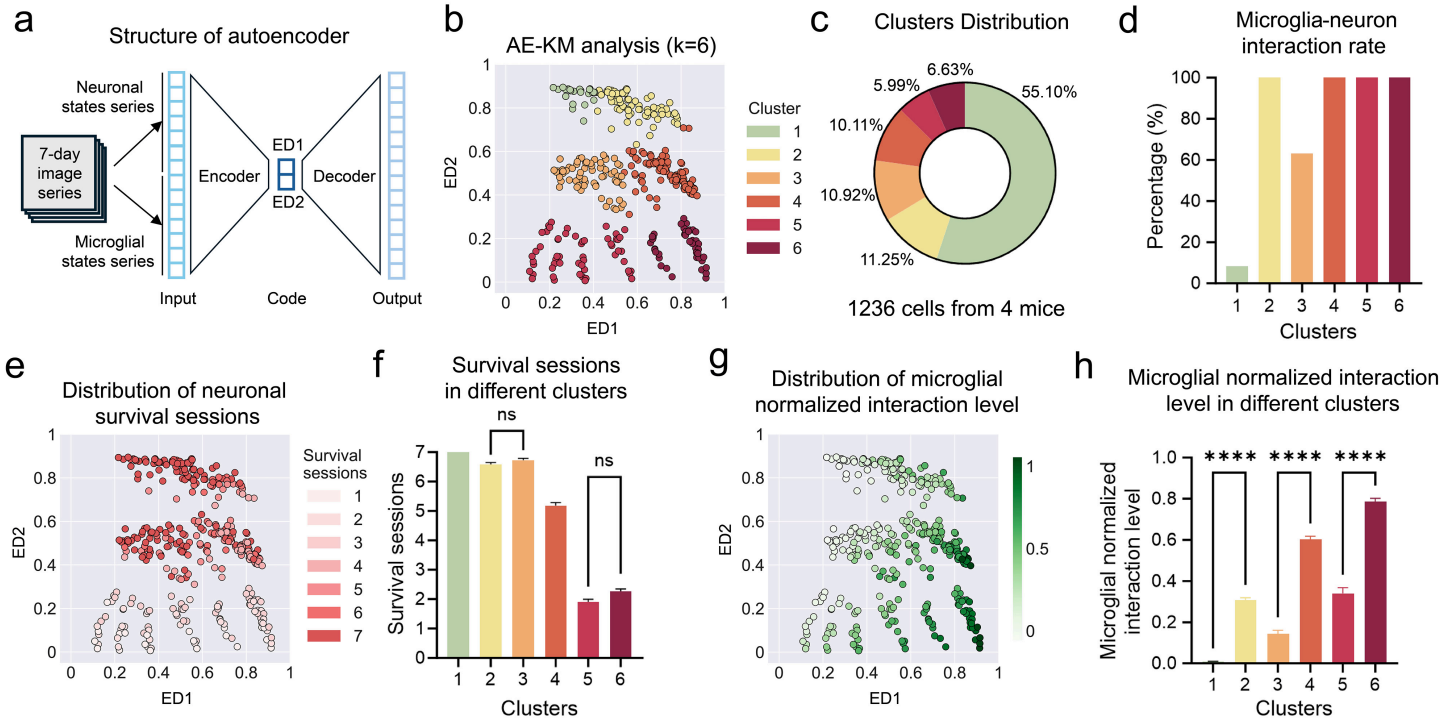


Figure 2

Latent-state mapping reveals trajectories of neuronal degeneration and microglial surveillance in TDP-43 proteinopathy. a, Schematic of the autoencoder architecture compressing 14-dimensional joint state sequences into a 2D latent space (ED1 and ED2). **b**, Identification of six distinct clusters via K-means clustering in the latent space. **c**, **d**, Population distribution of neuronal clusters (**c**) and quantification of the microglia–neuron interaction rate within each cluster (**d**). **e**, **f**, Projection of survival duration onto the latent space (**e**) and its quantification across clusters (**f**), identifying the second encoded dimension (ED2) as the health-to-degeneration axis. **g**, **h**, Projection of normalized microglial interaction scores onto the latent space (**g**) and their quantification across clusters (**h**), identifying the first encoded dimension (ED1) as the axis of surveillance intensity. Data are mean ± s.e.m. ****, $p < 0.0001$; Welch's ANOVA followed by Dunnett's T3 multiple comparisons test.

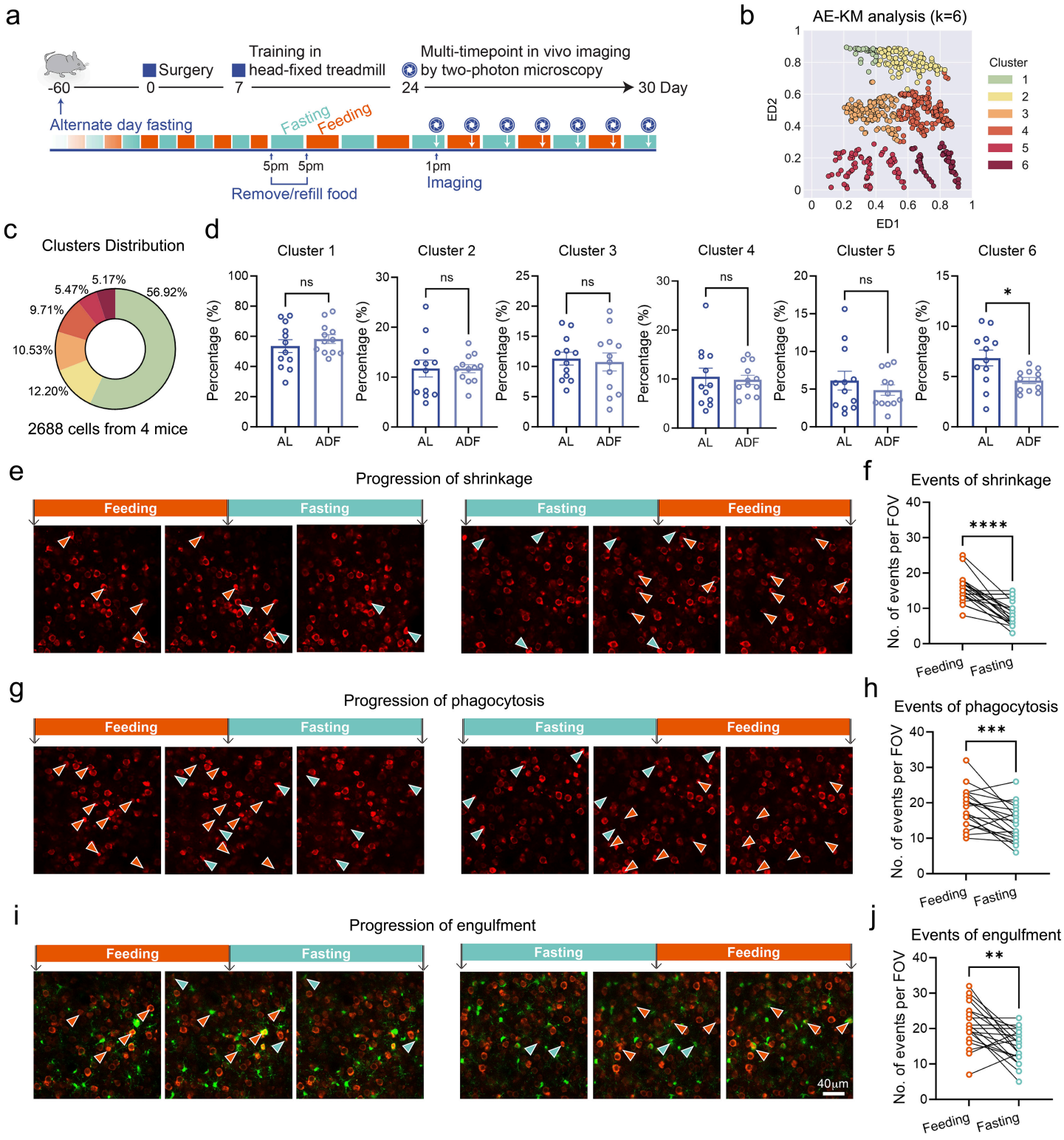


Figure 3

Alternate-day fasting induces phase-dependent oscillations in neurodegeneration and microglial reactivity. a, Schematic of the experimental design, illustrating the alternate-day fasting (ADF) regimen, surgical timeline, and daily longitudinal two-photon imaging protocol. **b**, Latent space projection of neuronal trajectories in the ADF cohort using the pre-trained autoencoder. **c**, **d**, Population distribution of neuronal clusters within the ADF cohort (**c**) and comparative quantification of cluster proportions

between AL and ADF groups (**d**). **e**, **g**, **i**, Representative time-lapse images capturing pathological events occurring between adjacent imaging sessions: neuronal shrinkage (**e**), microglial phagocytosis (**g**), and microglial engulfment (**i**). Scale bars, 40 μm. **f**, **h**, **j**, Pairwise quantification of the frequency of neuronal shrinkage (**f**), microglial phagocytosis (**h**), and microglial engulfment (**j**) during fasting versus refeeding windows. Data are mean ± s.e.m. *, $p < 0.05$, **, $p < 0.01$, ***, $p < 0.001$, ****, $p < 0.0001$. For **d**, unpaired two-tailed *t*-test with Welch's correction. For **f**, **h**, **j**, ratio paired *t*-test.

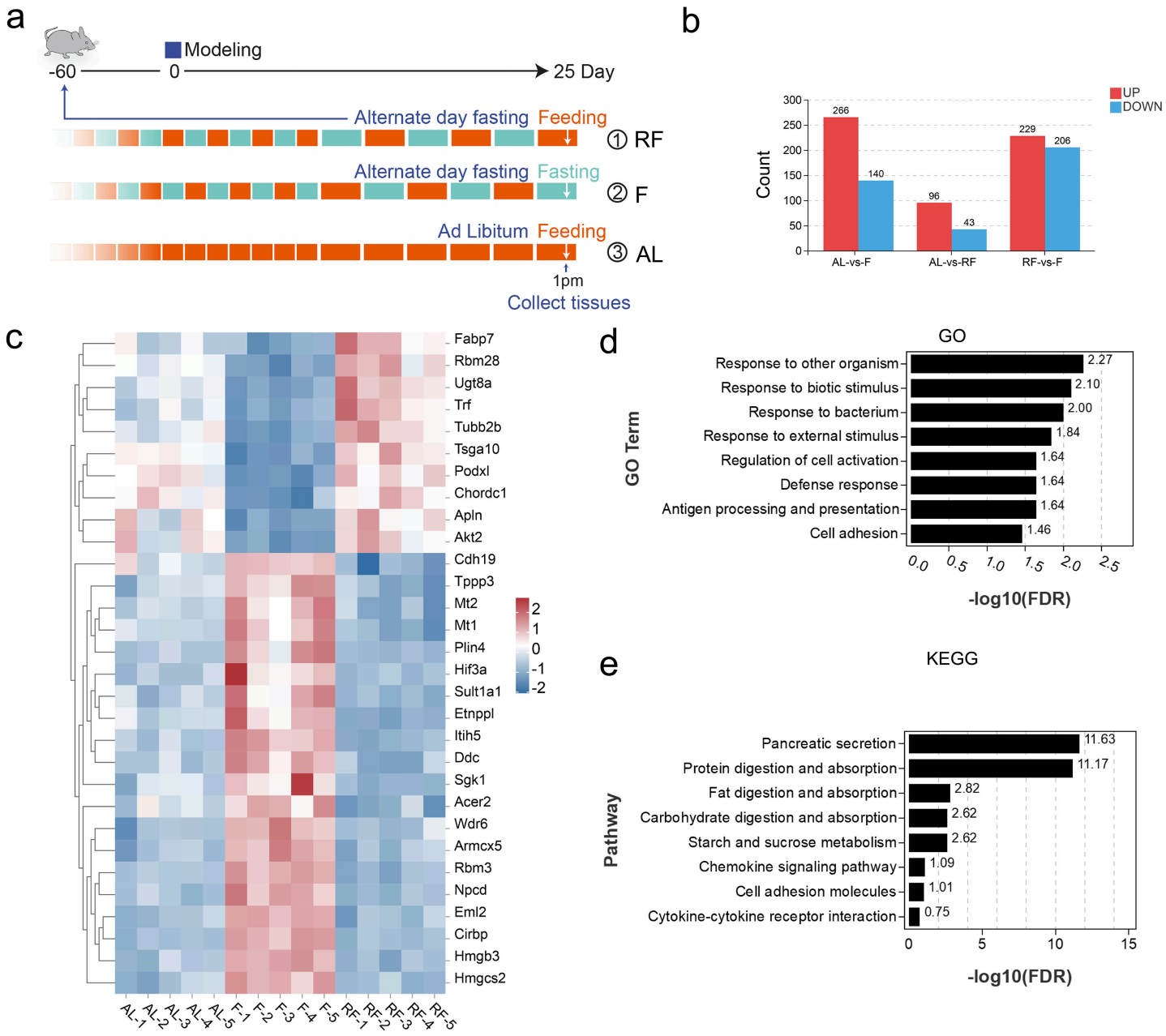


Figure 4

Refeeding triggers transcriptional overshoot and loss of fasting-induced neuroprotection. a, Schematic of the experimental design for transcriptomic analysis, comparing cortical tissues collected from mice in the fasting (F) or refeeding (RF) phase of ADF alongside *ad libitum* (AL) controls. **b**, Quantification of differentially expressed genes (DEGs) across pairwise comparisons, highlighting the high-magnitude

transcriptional reconfiguration between fasting and refeeding phases. **c**, Heatmap visualization of the top 30 DEGs differentiating the fasting and refeeding phases. The expression gradients reveal two distinct patterns: a "transcriptional overshoot" in metabolic and biosynthetic genes (e.g., *Fabp7*, *Akt2*) where RF levels surpass AL baseline, and a "rapid switch-off" of neuroprotective genes (e.g., *Hmgcs2*, *Mt1*) where RF levels revert to baseline. **d**, **e**, Functional enrichment analyses of refeeding-induced signatures. Gene Ontology (GO) analysis (**d**) identifies a predominant enrichment in immune-related processes, while Kyoto Encyclopedia of Genes and Genomes (KEGG) pathway analysis (**e**) confirms a dual molecular signature of intense metabolic processing coupled with inflammatory signaling.

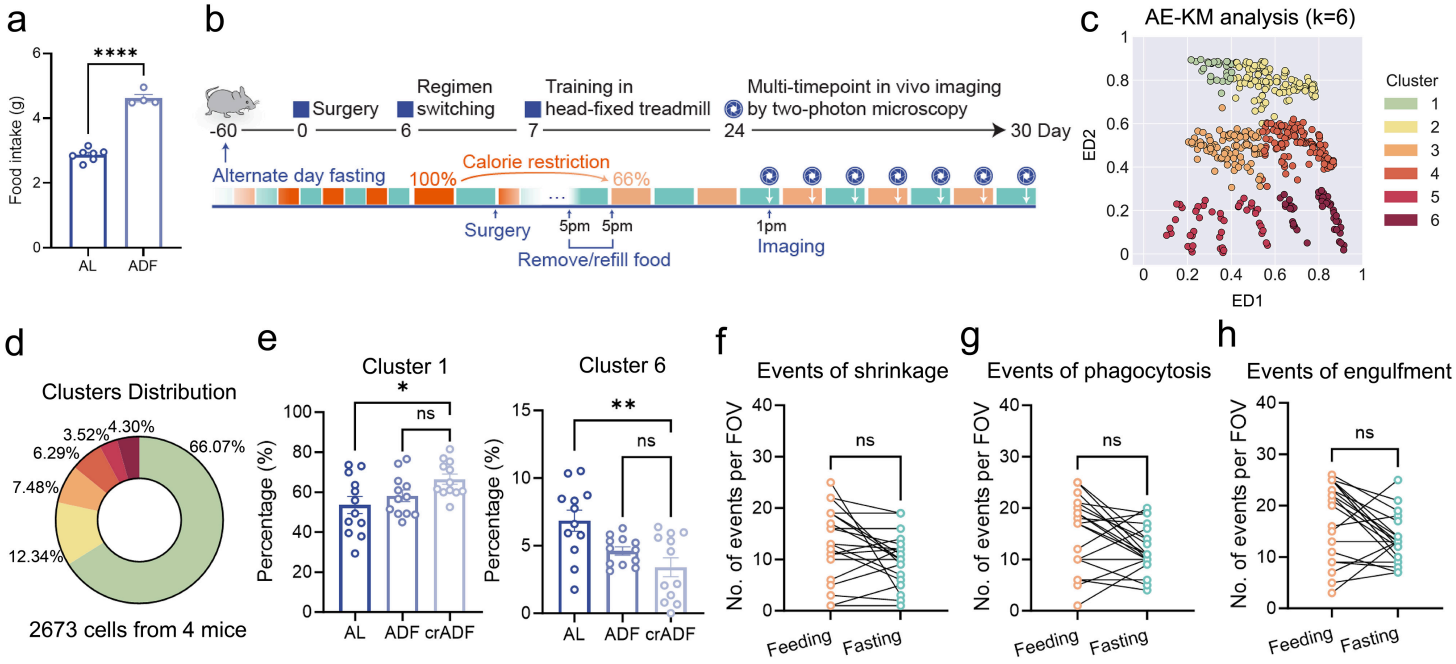


Figure 5

Calorie-restricted refeeding stabilizes neuronal trajectories during alternate-day fasting. a, Daily food intake showing compensatory hyperphagia in the standard ADF group relative to ad libitum (AL) controls. **b**, Experimental design illustrating the calorie-restricted alternate-day fasting (crADF) regimen, surgical timeline, and longitudinal two-photon imaging schedule. **c**, **d**, Latent space projection of neuronal trajectories in the crADF cohort (**c**) and the resulting population distribution of neuronal clusters (**d**). **e**, Comparison of the proportions of homeostatic (Cluster 1) and severely degenerative (Cluster 6) neurons across AL, ADF, and crADF groups. **f**–**h**, Pairwise quantification of the frequency of neuronal shrinkage (**f**), microglial phagocytosis (**g**), and microglial engulfment (**h**) during fasting versus refeeding windows in the crADF cohort. Note the abolition of phase-dependent volatility under caloric restriction. Data are mean ± s.e.m. *,$p < 0.05$, **, $p < 0.01$, ****, $p < 0.0001$. For e, Brown-Forsythe and Welch ANOVA tests followed by Dunnett's T3 multiple comparisons test. For f–h, ratio paired t-test.

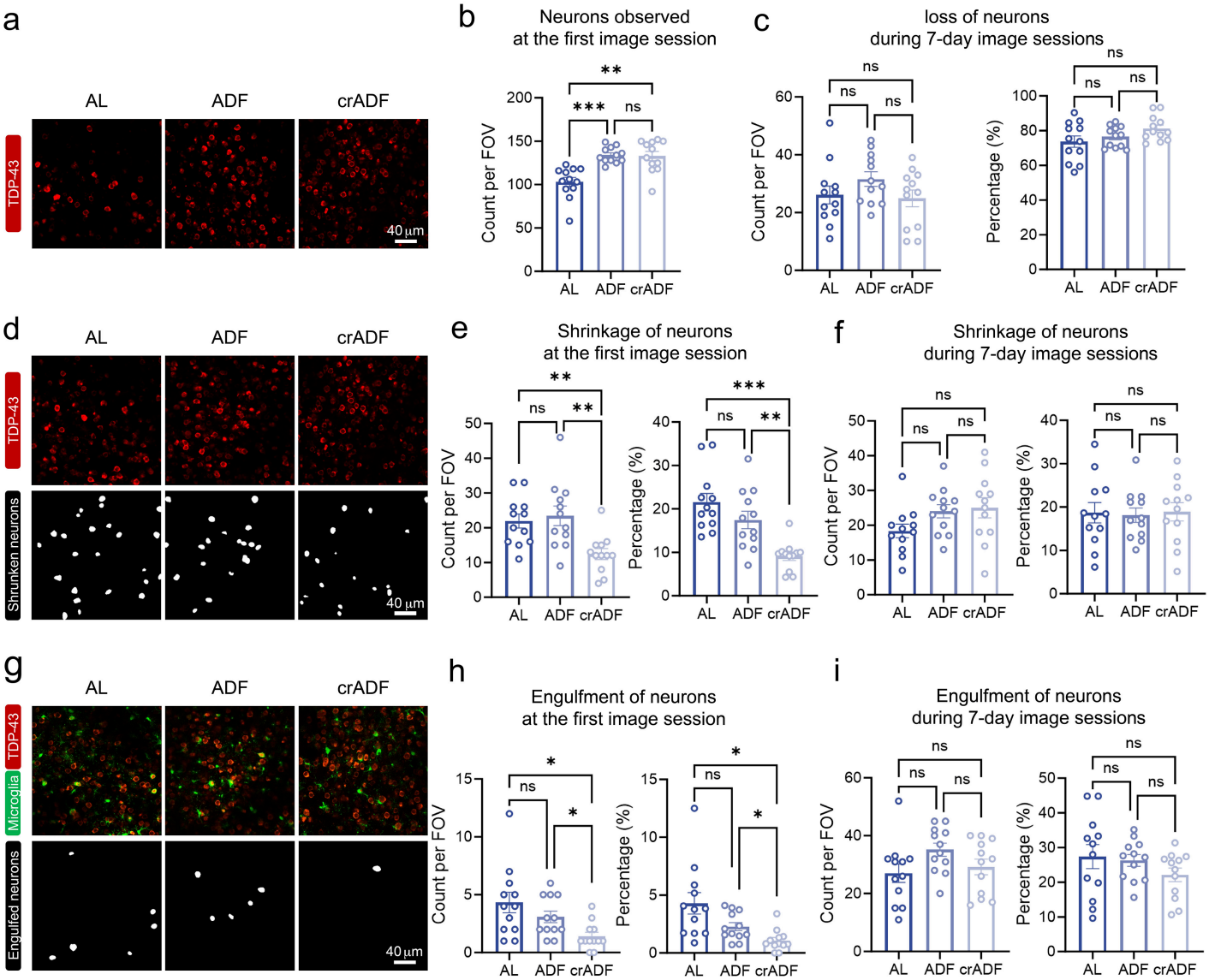


Figure 6

Comparative efficacy of crADF in mitigating acute and cumulative neurodegenerative pathology. a, Representative images of cortical fields in AL, ADF, and crADF cohorts. **b**, Quantification of the total number of neurons per field of view (FOV) on Day 1 across AL, ADF, and crADF groups. **c**, Quantification of the number and proportion of neuron loss (phagocytosed neurons) observed per FOV over the 7-day imaging window. **d**, Representative images highlighting shrunken neurons (arrowheads) in AL, ADF, and crADF cohorts. **e**, **f**, Quantification of the count and proportion of shrunken neurons assessed on Day 1 (**e**) and cumulatively over the 7-day imaging window (**f**). **g**, Representative images showing microglial engulfment of neurons in AL, ADF, and crADF cohorts. **h**, **i**, Quantification of the count and proportion of engulfed neurons assessed on Day 1 (**h**) and cumulatively over the 7-day imaging window (**i**). Note that crADF significantly mitigates both the initial disease burden and the cumulative neuronal loss compared to standard ADF. Data are mean ± s.e.m. *, $p < 0.05$, **, $p < 0.01$, ***, $p < 0.001$, statistical significance was assessed using Brown-Forsythe and Welch ANOVA tests followed by Dunnett's T3 multiple comparisons test.